From lattice Hamiltonians to tunable band structures by lithographic design

Athmane Tadjine, Guy Allan, and Christophe Delerue*
IEMN, UMR CNRS 8520, Lille, France
(Received 19 May 2016; revised manuscript received 21 July 2016; published 29 August 2016)

Recently, new materials exhibiting exotic band structures characterized by Dirac cones, nontrivial flat bands, and band crossing points have been proposed on the basis of effective two-dimensional lattice Hamiltonians. Here, we show using atomistic tight-binding calculations that these theoretical predictions could be experimentally realized in the conduction band of superlattices nanolithographed in III-V and II-VI semiconductor ultrathin films. The lithographed patterns consist of periodic lattices of etched cylindrical holes that form potential barriers for the electrons in the quantum well. In the case of honeycomb lattices, the conduction minibands of the resulting artificial graphene host several Dirac cones and nontrivial flat bands. Similar features, but organized in different ways, in energy or in k-space are found in kagome, distorted honeycomb, and Lieb superlattices. Dirac cones extending over tens of meV could be obtained in superlattices with reasonable sizes of the lithographic patterns, for instance in InAs/AlSb heterostructures. Bilayer artificial graphene could be also realized by lithography of a double quantum-well heterostructure. These new materials should be interesting for the experimental exploration of Dirac-based quantum systems, for both fundamental and applied physics.

DOI: 10.1103/PhysRevB.94.075441

I. INTRODUCTION

Nowadays, many popular research topics in condensed matter are inspired by the physics of graphene. Among its outstanding properties, its low-energy excitations are massless Dirac fermions, which enable the realization of quantum electrodynamics experiments on a laboratory table [1]. The hope of manipulating relativistic fermions in condensed matter has led to intensive research for alternative two-dimensional (2D) Dirac materials [2–4]. Soon after the discovery of graphene [5,6], silicene and germanene were predicted as 2D Dirac materials [7]. Furthermore, a connection between the honeycomb geometry and the appearance of Dirac cones has been made, leading to the concepts of artificial graphene and Dirac matter that presently receive huge attention [8].

In this context, several groups have proposed a top-down approach to fabricate artificial graphene on the basis of a 2D electron gas confined in a semiconductor heterostructure (quantum well) [9–14]. The idea is to apply a potential modulation in order to confine the electrons on a honeycomb lattice since it has been shown theoretically that massless Dirac fermions could be generated near the corner of the supercell Brillouin zone [9,10,13]. Pioneering experimental works in this field used a modulation-doped AlGaAs/GaAs heterostructure subjected to a lateral potential modulation generated by remote gates periodically ordered on a hexagonal lattice [10–14]. However, direct evidence of massless Dirac fermions has not yet been obtained, mainly due to the small bandwidth ($\ll$1 meV), which cannot overcome temperature and disorder effects [14].

Another unexpected way to build artificial graphene has been recently discovered by employing colloidal semiconductor nanocrystals as artificial atoms [15–17]. The oriented-attachment of the nanocrystals spontaneously forms long-range ordered honeycomb lattices. Theoretical studies of these structures have predicted the presence of Dirac cones and other interesting features, such as nontrivial flat bands in their energy band dispersion [18–20].

On the theoretical side, different types of 2D Dirac materials have been predicted [21–29]. In addition, several studies have shown that, in principle, Dirac cones could be obtained in other types of lattices, such as the kagome [30–32] and Lieb [33–39] lattices. A recent theoretical work has explained, based on a symmetry approach, how Dirac cones could be found beyond the honeycomb lattice [40]. In spite of this richness of predicted materials, their experimental realization remains quite challenging. Many interesting properties that have been predicted on the basis of effective tight-binding Hamiltonians could be potentially investigated using ultracold atoms trapped in optical lattices. However, solid-state realizations of these model systems are still lacking.

In this paper, we theoretically propose experimentally feasible structures in which Dirac cones, nontrivial flat bands, and band crossing points can be present. These structures could be made by patterning superlattices in ultrathin films of III-V and II-VI semiconductors using nanoscale lithography. In these superlattices, our atomistic tight-binding calculations show that the conduction bands are composed of minibands characterized by energy dispersions, which have been previously derived from effective Hamiltonians.

Taking InAs as a model system, we study honeycomb lattices formed by etched cylinders arranged on a triangular lattice. We perform a systematic study by varying the main structural parameters in order to design experimentally realizable structures with optimum properties. We show that this lithographic approach opens a road towards other interesting lattices such as kagome and Lieb lattices. We also predict the existence of Dirac cones in a distorted honeycomb lattice, which has not been investigated so far. We extend these results to other III-V and II-VI semiconductor compounds. We also propose the realization of bilayer artificial graphene.

In the following, we will see that the main requirement to obtain these effects is the confinement of the electrons in the superlattice vertices, and a strong connection between these vertices. In fact, the confinement of the electrons creates

*christophe.delerue@iemn.univ-lille1.fr

discrete energy levels, which can be assimilated to those of artificial orbitals that generate the minibands under the effect of nearest-neighbor coupling. As a consequence, the superlattices of these artificial orbitals can be described by simple effective tight-binding models. Reciprocally, this study shows the possibility to go from effective Hamiltonians to reality out of lithographed structures that can be massively produced.

II. METHODOLOGY

A. Geometry of the superlattices

We consider superlattices made from a semiconductor (mostly InAs) quantum well of thickness t in which electrons are injected by (remote) doping or electrostatic gating. We introduce in the layer a periodic array of holes (mostly cylindrical), which form potential barriers for the electrons. These holes can be realized by etching the layer using e-beam lithography. Except otherwise stated, the surfaces of the processed semiconductor layer are passivated by pseudo-hydrogen atoms that push the surface states far from the energy gap region. In these conditions, the electrons are entirely confined in the remaining parts of the layer. The electrons, which are totally free to move in two directions in the pristine quantum well, are periodically scattered by the etched holes. This leads to the formation of minibands in the conduction band of the superlattices.

Several types of superlattices have been studied (Fig. 1). The first one (discussed in Sec. III) is a square superlattice made by etched cylindrical holes arranged on a square lattice [Fig. 1(a)]. The second type (Sec. IV) results from the hexagonal arrangement of the etched cylinders [Fig. 1(b)]. It forms an artificial graphene since the electrons are mostly confined within the vertices of the structure that behave like artificial atoms coupled together to form a honeycomb. In both cases, the main structural parameters are the diameter D of the holes, and the distance d between the centers of the holes (which also corresponds to the superlattice parameter).

We have also explored four more exotic superlattices discussed in Sec. V. The kagome (Sec. V A) and distorted honeycomb (Sec. V B) superlattices have a hexagonal symmetry with respectively three and six artificial atoms per unit cell [Figs. 1(c) and 1(d)]. The kagome is made by adding to the honeycomb structure a second type of holes with smaller diameter that are arranged as depicted in Fig. 1(c). The distorted honeycomb is obtained from the honeycomb by considering a unit cell of three holes and by changing the shape of holes from circular to ellipsoidal. The three ellipses per unit cell are rotated by 120° from each other. The Lieb lattice (Sec. V C) is characterized by three artificial atoms in a square unit cell and is obtained by mixing two different cylindrical holes of diameter D and D' [Fig. 1(e)]. The detuned honeycomb (Sec. V D) is obtained by detuning the hole sizes as depicted in Fig. 1(f).

The out-of-plane axis corresponds to the ⟨001⟩ crystallographic direction for square and Lieb superlattices, to the ⟨111⟩ direction for honeycomb, kagome, distorted, and detuned honeycomb superlattices. In these conditions, the superlattice vectors are consistent with the underlying microscopic zinc-blende lattice of the semiconductor.

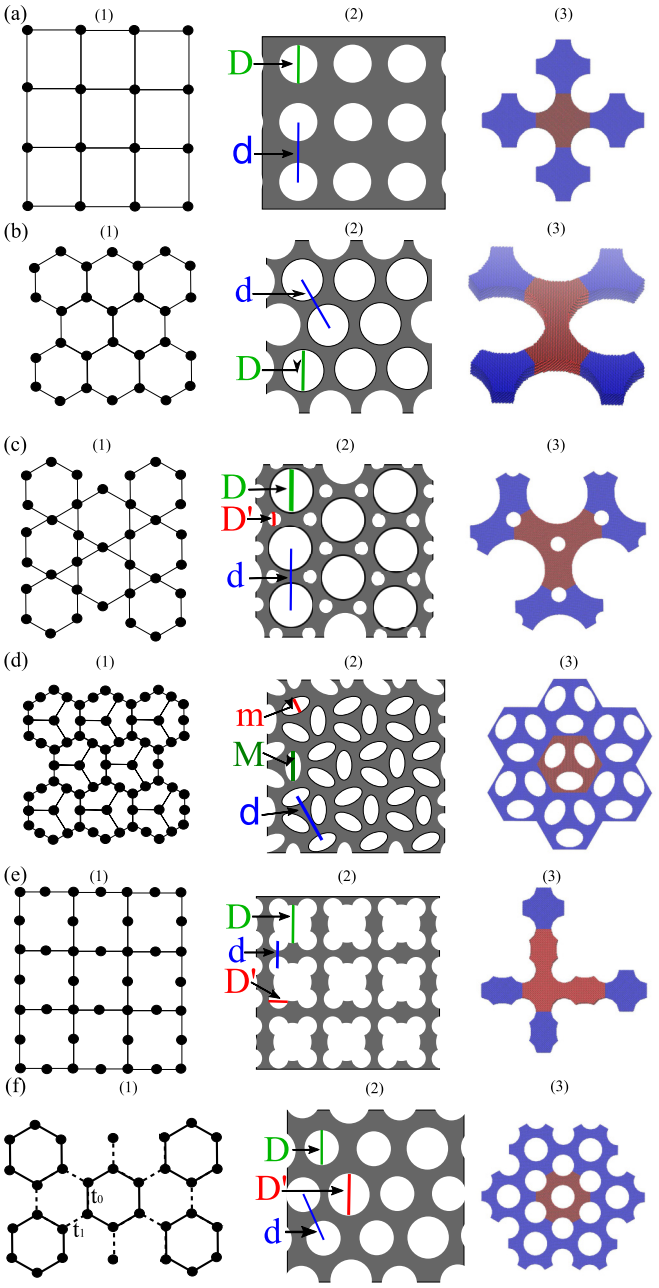

FIG. 1. Geometry of the studied superlattices. Schematics showing the reproduction of the original atomic lattice (1) by etching holes in a semiconductor thin film (2) and the unit cell of the actual studied system (3). (a) Square, (b) honeycomb, (c) kagome, (d) distorted honeycomb, (e) Lieb, and (f) detuned honeycomb. The atoms (not distinguishable at this scale) of the unit cell are in red and those from next-neighbor cells (for periodicity) are in blue. The main structural parameters are: for (a) and (b), D is the diameter of the holes and d is the distance between them; for (c), (e), and (f), D and D' are the diameters of the two different hole sizes and d is the distance between them; for (d), M is the length of the ellipse's major axis and m is the length of its minor one, d is the distance between two holes taken at the intersection of major and minor axes. The typical sizes of the etched holes for the studied structures range from 7–21 nm and the distances between them from 12–38 nm.

B. Tight-binding calculations

An atomistic tight-binding method is used to compute the electronic band structures. Each atom from the zinc-blende structure is described by a double set of $sp^3d^5s^*$ atomic orbitals, including the spin degree of freedom. Only first-nearest-neighbor interactions are considered and the orbitals are assumed to be orthogonal. The Hamiltonian matrix is calculated using the tight-binding parameters derived in Ref. [41] for InAs, InP, GaAs, and AlSb, in Ref. [42] for CdTe, and in Appendix A for InSb. Those parameters are fitted in order to reproduce the bulk band structure that is obtained by *ab initio* calculations. There is no free parameter in the calculations. The spin-orbit coupling is described by intra-atomic Hamiltonian matrix elements in the p sector. The surface states are pushed far from the energy gap using a surface passivation with pseudo-hydrogen atoms.

For structures that can be realistically fabricated by top-down lithography, the number of atoms per unit cell can be huge, even though the etched holes contribute to reduce it. We have investigated systems containing up to 1.3×10^5 atoms and 2.6×10^6 atomic orbitals. Because of these large numbers, only the lowest conduction minibands are calculated using the numerical methods described in Ref. [43]. These methods are based on the Jacobi-Davidson algorithm, which allows us to compute only few eigenvalues (and corresponding eigenstates) near a given energy σ. In this work, σ is always set in the bulk gap, near the valence band edge. By convention, the zero of energy is fixed at the top of the valence band of bulk systems.

Only the conduction bands of the superlattices are investigated in the present work because they can be easily manipulated by tuning quantum confinement effects. The situation is much more complex in the valence band because of the presence of heavy-hole, light-hole, and split-off bands, which are coupled in confined structures. Therefore, the valence bands will not be discussed here, even if previous theoretical works have shown that the strong spin-orbit coupling induces exotic quantum phases, such as the quantum spin Hall effect predicted in semiconductors on which a potential with hexagonal symmetry is superimposed [44] or in honeycomb superlattices of colloidal CdSe nanocrystals [17,18].

III. ARTIFICIAL SQUARE LATTICE

To understand the mechanism of formation of artificial superlattices in etched semiconductor thin films, we have studied the simple case of a square superlattice. Figure 2(a) shows the conduction band structure obtained for an InAs film with $D = 17.6$ nm, $d = 24.2$ nm, and $t = 6.1$ nm. We can distinguish two manifolds of minibands. Their behavior can be understood as follows.

The electrons are mainly confined within the vertices of the square superlattice, this results in discrete energy levels whose coupling generates the minibands. The two lowest levels have a s-like wave-function envelope [Fig. 2(b)], the four others exhibit two opposite lobes and a single node in the x-y lattice plane, which indicate that their wave-function envelopes are $p_{x,y}$-like. Due to the strong confinement in the vertical direction (z), the envelope wave functions are more 2D than 3D, the p_z states are higher in energy (not shown),

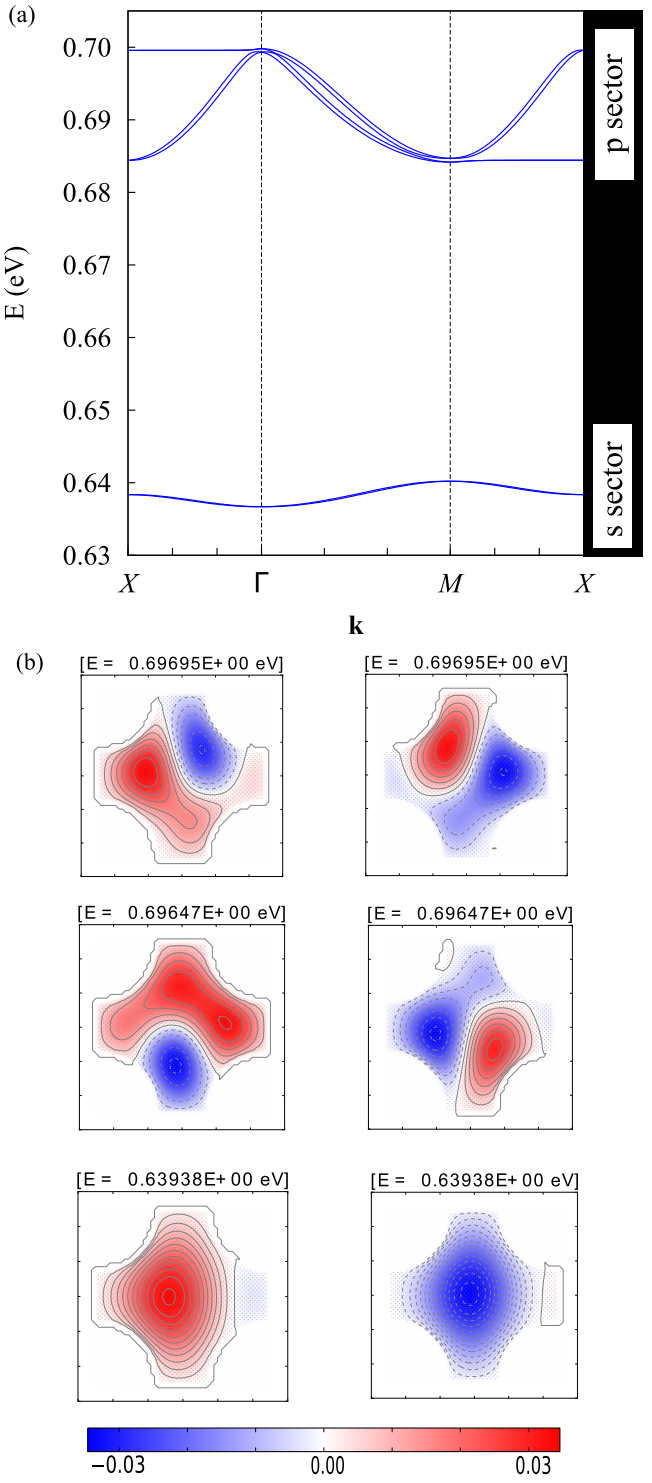

FIG. 2. Results for a square superlattice in an InAs layer. (a) Lowest six conduction minibands for the square superlattice vs the wave vector **k** along the path shown in Appendix B for a structure with $d = 24.2$ nm, $D = 17.6$ nm, and $t = 6.1$ nm. (b) Wave functions of the six lowest conduction states in an isolated InAs nanocrystal defined by a single unit cell of the superlattice. The two lowest states of energy $E = 0.63938$ eV have a 2D s-like envelope wave function while the four higher states ($E = 0.69647$ eV and $E = 0.69695$ eV) have a 2D $p_{x,y}$-like envelope wave function. The small splitting between the two manifolds of p states comes from the spin-orbit coupling.

and the s-like and $p_{x,y}$-like states are squeezed along the z axis. The band structure presented in Fig. 2(a) is the expected one for a simple tight-binding Hamiltonian with s and $p_{x,y}$ orbitals per atom, as already shown for square superlattices of colloidal nanocrystals [45]. Figure 2(b) shows that the p states are not pure p_x and p_y states, but they are mixed and their degeneracy is lifted due to the spin-orbit coupling. The latter is also responsible for the small splitting of the bands visible in the p sector [Fig. 2(a)].

IV. HONEYCOMB SUPERLATTICES

A. Model system: InAs superlattices

Figure 3 presents results for an InAs honeycomb superlattice, including a typical band structure that we predict for a wide range of sizes [Fig. 3(a)]. This band structure exhibits several Dirac cones and nontrivial flat bands. All minibands are doublets of quasidegenerate bands. The behavior of the lowest minibands can also be understood by considering each vertex of the superlattice as an artificial atom. Figure 3(b) shows that the envelope wave function of the two lowest states in each artificial atom is s-like, while the one of the four other states above in energy is p-like. Taking into account that the superlattice unit cell is composed of two artificial atoms, these s and $p_{x,y}$ states are at the origin of the twelve lowest bands (including spin degeneracy) forming two manifolds.

Due to the honeycomb geometry, the s states (of the artificial atoms) give rise to bands with a Dirac cone at the K point. Their energy dispersion behaves like the π and π^* bands in real graphene. $p_{x,y}$ states also form π-like bands in addition to nontrivial flat bands. The hexagonal symmetry induces a frustration of the $p_{x,y}$ artificial-atom orbitals resulting in destructive interferences that cause the appearance of these flat bands [46,47]. The flat bands are connected to the π bands just at Γ. These band crossing points are protected by the topology and the symmetry of the lattice [40,47,48]. The splitting between the π-π^* bands at the M point (hereafter referred to as the bandwidth), a measure of the band dispersion, varies significantly with the ratio D/d, for both s and $p_{x,y}$ bands [Fig. 4(a)]. In the p sector, it is inversely proportional to D/d due to the weakening of the coupling between the artificial-atom orbitals. For D/d smaller than 0.6, the π-like bands in the p sector mix with higher-energy bands [Fig. 4(b)]. In the s sector, the bandwidth is reduced at small D/d due to the increasing coupling between s and p states. Nevertheless, splittings at the M point above 10 meV can be obtained with reasonable (regarding lithography techniques) hole sizes [Fig. 4(a)].

In absence of kinetic energy, nontrivial flat bands are interesting for the study of correlated electron systems. Theoretical studies have predicted that they could host exotic quantum phases, such as the fractional quantum Hall phase in presence of spin-orbit coupling [49–51]. Figure 4(b) shows that these nontrivial flat bands no longer exist for small values of D/d due to the coupling with higher bands.

The bands above the $p_{x,y}$ bands in Fig. 3(a) come from 2D d orbitals of the artificial atoms. They are characterized by a well-defined Dirac cone in π-like bands, a flat band above the

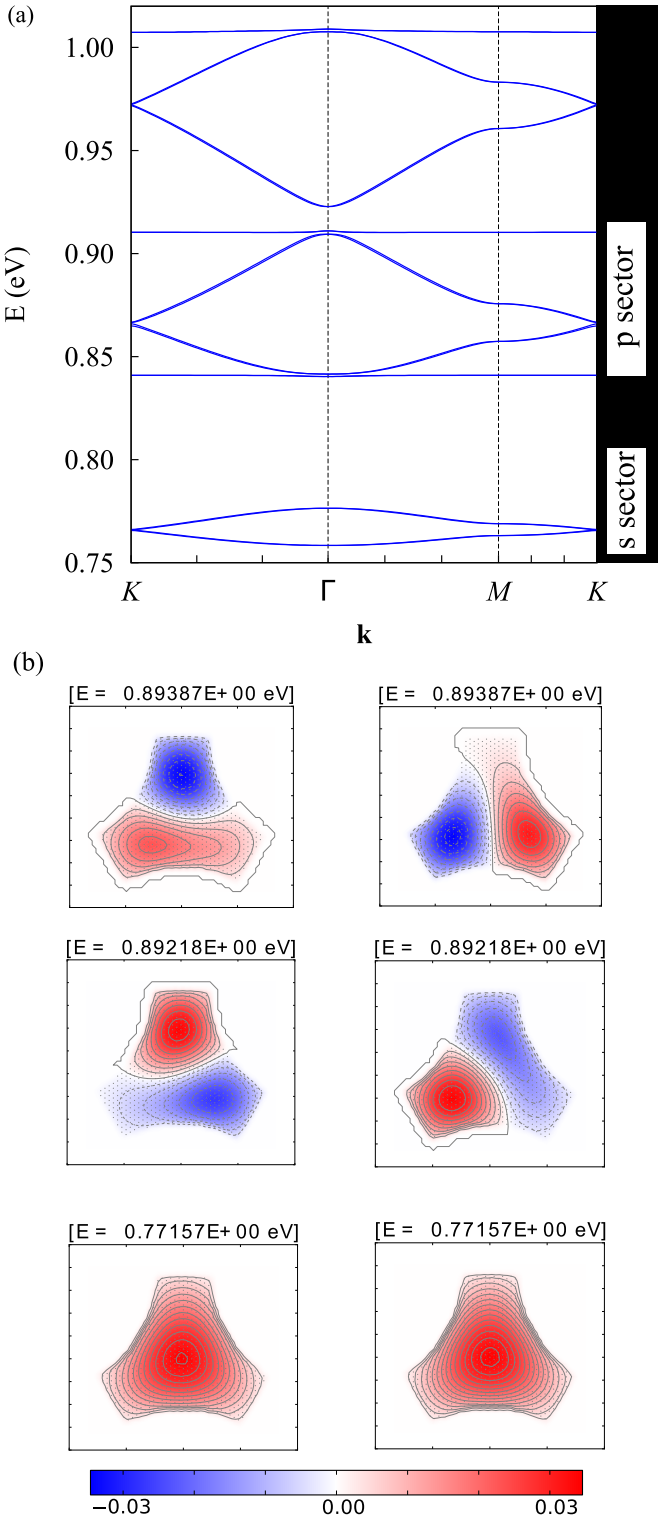

FIG. 3. Results for a honeycomb superlattice in an InAs layer. (a) Lowest conduction minibands for the honeycomb superlattice vs the wave vector **k** along the path shown in Appendix B for a structure with $d = 24.5$ nm, $D = 19.7$ nm, and $t = 3.9$ nm. (b) Wave functions of the six lowest states confined in an isolated nanocrystal defined by half a single unit cell of the superlattice, i.e., as found at each superlattice vertex. The two lowest-energy states of energy $E = 0.77157$ eV have a 2D s-like envelope wave function while the four higher-energy states ($E = 0.89218$ eV and $E = 0.89387$ eV) have a 2D $p_{x,y}$-like envelope wave function.

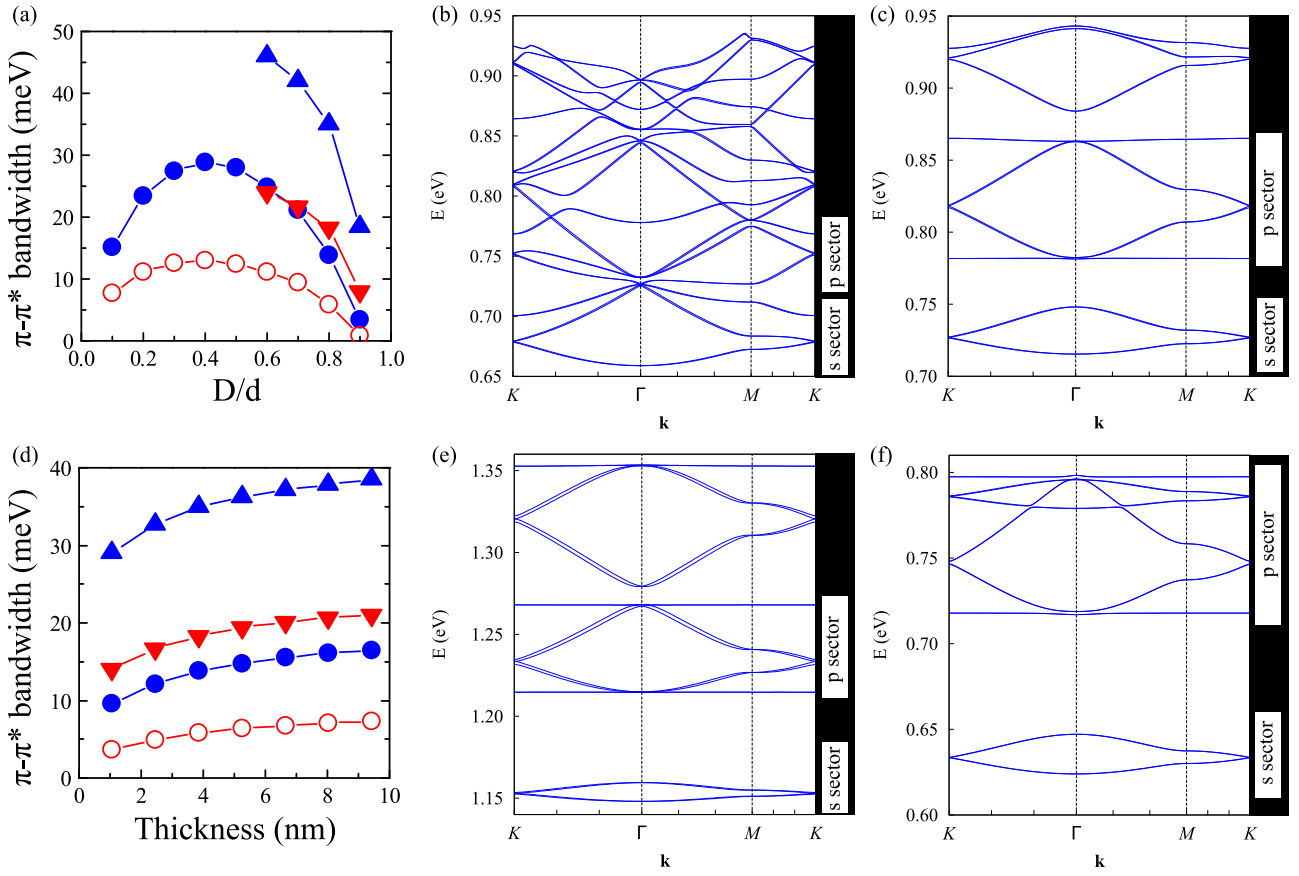

FIG. 4. Evolution of the band structure with structural parameters for honeycomb superlattices. (a) Evolution of π-π^* bandwidth at the M point with the ratio D/d, where D is the diameter of the holes and d the distance between two consecutive holes. The film thickness is set at $t = 3.9$ nm. Blue •: s sector bands with $d = 15.6$ nm, red ○: s sector bands with $d = 24.5$ nm; blue ▲: p sector bands with $d = 15.6$ nm, red ▼: p sector bands with $d = 24.5$ nm. (b) Lowest conduction bands for $d = 24.5$ nm, $D = 5.0$ nm ($D/d = 0.2$), and $t = 3.9$ nm. (c) Lowest conduction bands for $d = 24.5$ nm, $D = 17.3$ nm ($D/d = 0.7$), and $t = 3.9$ nm. (d) Evolution of π-π^* bandwidth at the M point with the thickness t of the film. The ratio D/d is set at 0.8. Blue •: s sector bands with $d = 15.6$ nm, red ○: s sector bands with $d = 24.5$ nm; blue ▲: p sector bands with $d = 15.6$ nm, red ▼: p sector bands with $d = 24.5$ nm. (e) Lowest conduction bands for $d = 24.5$ nm, $D = 19.7$ nm, and $t = 1.1$ nm. (f) Lowest conduction bands for $d = 24.5$ nm, $D = 19.7$ nm, and $t = 9.4$ nm.

upper π band, and a crossing point between the two bands at Γ. This shows the multiorbital character of these artificial superlattices that is certainly hard to find in real materials.

The evolution of the bandwidth in the s and p sectors vs the thickness of the film is smooth and presents a quasiplateau [Fig. 4(d)]. However, there is a missing information in this representation, as shown in Figs. 4(e) and 4(f). The higher-energy quantum well states (somehow p_z-like, with a node along the vertical direction), induced by the confinement along the perpendicular axis, also couple together to create minibands. At increasing thickness, these sub-bands have lower energy and mix with the $p_{x,y}$ ones. If one just wants to investigate the s bands, this effect does not represent any issue. However, for the investigation of $p_{x,y}$ bands, film thicknesses smaller than ∼10 nm are required to avoid these effects.

Finally, we notice that the bigger is the hole size, the smaller is the bandwidth. This was expected since the confinement is weaker when the size of the artificial atoms increases. Nevertheless, we choose in the rest of this paper to focus on hole sizes attainable experimentally ($\gg$10 nm).

B. Superlattices made from other compounds

From the explanation of the mechanism leading to Dirac and nontrivial flat bands, we can see that the nature of the semiconductor compound is not crucial, provided that it is characterized by a single conduction valley with a relatively small effective mass that enhances confinement effects. We show in this section nonexhaustive results on other III-V and II-VI compounds, namely InP [Fig. 5(a)], GaAs [Fig. 5(b)], InSb [Fig. 5(c)], and CdTe [Fig. 5(d)]. For the sake of comparison, we consider superlattices with $D/d \approx 0.8$.

The band structures predicted for other semiconductors (Fig. 5) are basically the same as for InAs [Fig. 4(c)], and they present comparable bandwidths even if the largest ones are found in materials with the smaller effective mass (InSb, InAs). However, the band dispersions are slightly different in the InSb system. Due to a strong spin-orbit coupling and a broken inversion symmetry ($\langle 111\rangle$ and $\langle \bar{1}\bar{1}\bar{1}\rangle$ directions are not equivalent), the Rashba spin-orbit coupling induces a visible spin splitting of the bands, especially in the p sector. In the next sections, we will only show results for InAs systems, but one

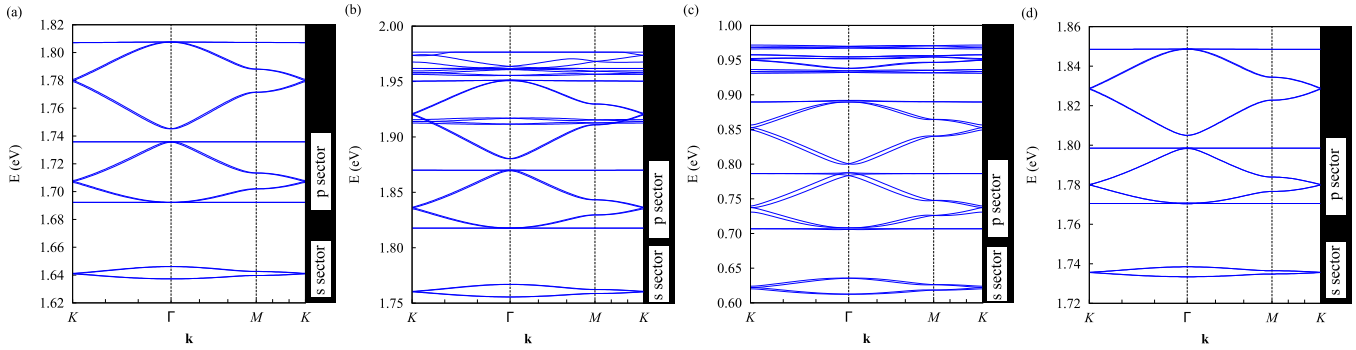

FIG. 5. Results for honeycomb superlattices with different III-V and II-VI compounds. Lowest conduction bands for (a) InP with $d = 23.7$ nm, $D = 19.0$ nm, and $t = 3.7$ nm, (b) GaAs with $d = 22.8$ nm, $D = 18.3$ nm, and $t = 3.6$ nm, (c) InSb with $d = 26.2$ nm, $D = 21.0$ nm, and $t = 4.1$ nm and (d) CdTe with $d = 26.2$ nm, $D = 21.0$ nm, and $t = 4.1$ nm.

has to keep in mind that it is possible to recover similar ones with other III-V and II-VI compounds. Thus, the number of interesting structures using this lithographic approach is quite large.

V. TOWARDS EXOTIC STRUCTURES BEYOND THE HONEYCOMB LATTICE

In this section, we investigate more exotic structures made by the lithographic approach. We show that it is possible to reproduce band structures originally predicted using effective Hamiltonians in different types of lattices. We will see that the lithographic technique allows us to design artificial lattices that mimics the behavior of their atomic counterparts, which remain at the moment at the level of model systems. We also consider an original lattice for which interesting features are found.

A. Kagome

We have investigated the band structure of an artificial kagome lattice made from an InAs films. The geometry of the superlattice is described in Fig. 1(c). The Brillouin zone is the same as for the honeycomb (Appendix B). The effective tight-binding model for the kagome lattice with a single orbital per site and a constant hopping term between nearest-neighbor orbitals has been widely studied [30–32]. Three spin-degenerate bands are predicted, two behave as the π-π^* bands of graphene hosting a Dirac cone at the K point, and a nontrivial flat band crosses the π^* band just at the Γ point. Thus, the spectrum consists of a flat band at $E = E_s + 2t$ and two dispersive bands written as [30]

$$E_{\pm}(\mathbf{k}) = E_s + t[-1 \pm \sqrt{4A(\mathbf{k}) - 3}] \quad (1)$$

with $A(\mathbf{k}) = \cos^2 k_1 + \cos^2 k_2 + \cos^2 k_3$, where E_s is the on-site orbital energy, t the first-nearest-neighbor hopping energy, and $k_n = \mathbf{k}.\mathbf{a_n}$ with $\mathbf{a_1} = (1,0)a$, $\mathbf{a_2} = \frac{(1,\sqrt{3})a}{2}$, and $\mathbf{a_3} = \mathbf{a_2} - \mathbf{a_1}$, the three nearest-neighbor vectors of length a.

The band structure of Fig. 6(a) presents this expected behavior in the s sector and a good agreement with the effective tight-binding model is found (see Appendix D for the fitted parameter values). This emphasizes the fact that the artificial structure reproduces the lattice band structure. One can clearly observe an asymmetry between the bandwidth of the dispersive bands in the artificial structure, which is caused by the interaction with higher bands that are not taken into account in the effective Hamiltonian.

For the investigated structure size, the π-π^* bandwidth at the Γ point is equal to 10.4 meV. The upper band in the s sector is extremely flat, showing that the effective coupling between artificial atom s orbitals are mainly restricted to nearest-neighboring ones. The crossing point between the π^* band and the flat band at Γ is protected by the topology. In the p sector, a more complex dispersion is found due to the intermixing of the $p_{x,y}$ states present at the vertices in the cells.

B. Distorted honeycomb

As described in Sec. II A, we have designed a new type of lattice in the form of a distorted honeycomb [Fig. 1(d)]. This lattice has six artificial atoms per unit cell and bonds between them with different strengths and orientations. Figure 6(b) shows a s sector composed of six spin-degenerate bands. There are two manifolds of π-π^* bands, giving rise to two Dirac cones at K. In addition, there are two less dispersive bands in the s sector. For the studied sizes, the bandwidth at the Γ point of the first π-π^* manifold is equal to 25 meV while the bandwidth of the second one is equal to 54 meV. We have developed in Appendix C an effective tight-binding Hamiltonian, which reproduces the main features of the band structure presented in Fig. 6(b).

C. Lieb lattice

The Lieb lattice, characterized by three atoms in a square unit cell, has been studied both theoretically and experimentally, in the case of ultracold atoms in optical lattices, and in photonic lattices [33–39]. The effective tight-binding model for a single s orbital per site gives three bands with interesting features. If the on-site energy is the same on the three s orbitals of the unit cell, two bands cross at the M point, forming a Dirac cone. The third band is totally flat and intercepts the Dirac cone at the same point. This behavior at the M point can be described by a three-component quantum equation for pseudospin 1 fermions [34]. However, if the on-site energy for the atoms at the corners of the square lattice (denoted sites A) is not the same as for the atoms located at the bond centers (sites B), a gap opens up and the Dirac fermions acquire an

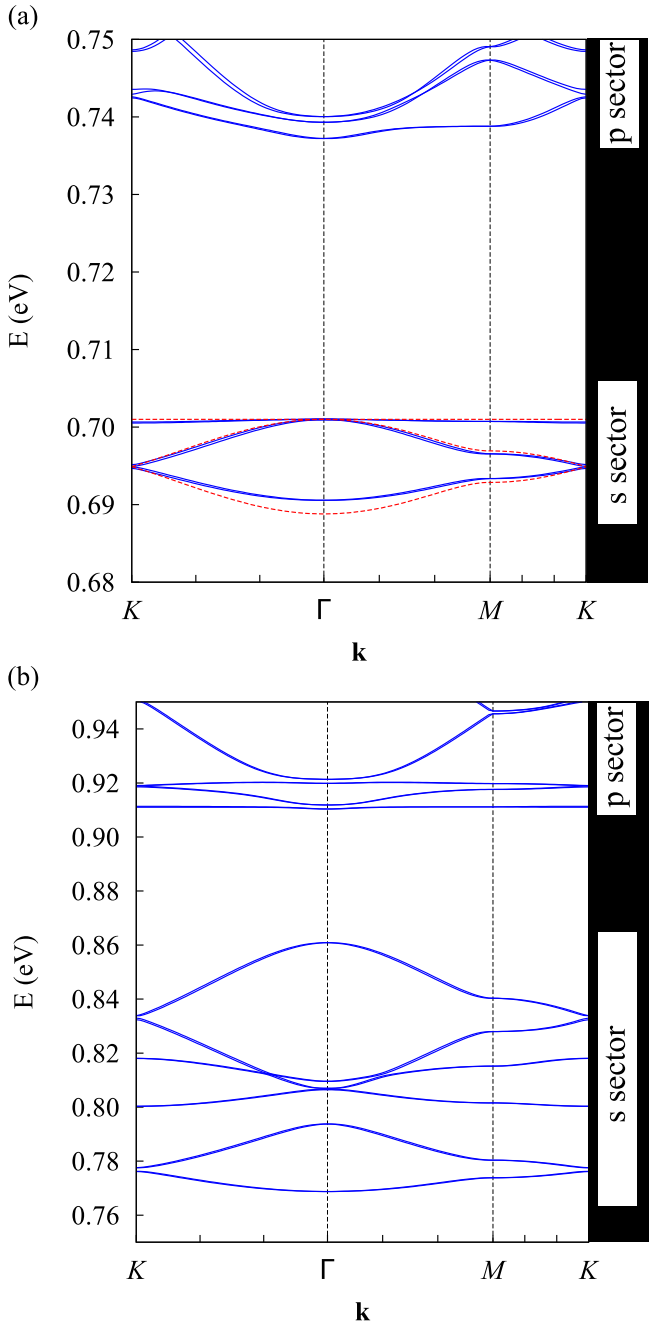

FIG. 6. Results for kagome and distorted honeycomb superlattices made from an InAs films. (a) Lowest conduction bands for the kagome superlattice with $d = 38.6$ nm, $D = 22.3$ nm, $D' = 6.7$ nm, and $t = 3.8$ nm. The dashed lines in the s sector show the results of the effective Hamiltonian. (b) Lowest conduction bands for the distorted honeycomb superlattice with $d = 26.1$ nm, $M = 12.5$ nm, $m = 8.7$ nm, and $t = 3.9$ nm.

effective mass [34]. Thus, the spectrum consists of a flat band at $E = E_s + \Delta$ and two dispersive bands

$$E_{\pm}(\mathbf{k}) = E_s \pm \sqrt{\Delta^2 + 4t^2\left[\cos^2\left(k_x\frac{a}{2}\right) + \cos^2\left(k_y\frac{a}{2}\right)\right]}, \tag{2}$$

where 2Δ is the difference between the on-site energies of sites A and B, E_s is their mean value, t the first-nearest-neighbor hopping energy, and a the lattice parameter.

We reproduce the Lieb lattice using two different hole sizes [Fig. 1(e)]. The resulting artificial atoms of sites A are characterized by four nearest neighbors, and those of sites B have only two nearest neighbors. The sites B are all equivalent due to the symmetry between [100] and [010] orientations. A typical band structure is shown in Fig. 7. As expected, we find three bands in the s sector but there is no Dirac cone because the on-site energy of the artificial atoms is, by construction, different on sites A and B. This leads to massive Dirac fermions at the M point [34]. However, the third band is remarkably flat and touches one of the other bands at the M point that is protected by the topology of the lattice. A good agreement with the effective tight-binding model is found (fitted parameters for the effective models are presented in Appendix D). As in kagome, an asymmetry exists in the two dispersive bands due to the coupling with higher bands that are missing in the effective Hamiltonian.

If one takes into account the next-nearest-neighbor hopping term in the effective Hamiltonian, the flat band becomes dispersive [52]. Thus, the presence of a flat band confirms that an effective nearest-neighbor coupling is sufficient to describe the band structure.

D. Detuned honeycomb

In addition to distortions, the lithographic approach also allows us to realize effective Hamiltonians with detuned hopping energies [t_0 and t_1, cf. Fig. 1(f1)]. In a recent paper, it was shown theoretically that by detuning the honeycomb lattice in a certain fashion, a gap opens up and a topological phase transition occurs [53]. We show in this section that it is possible to realize this detuning and to open the gap.

Starting from the honeycomb lattice, if one considers a unit cell of six atoms (i.e., three times bigger than the graphene one), then the π-π^* bands are folded as shown in Fig. 7(b). If one now enhances the coupling between these hexagons by taking $t_0 < t_1$, a gap opens up in the band structure [Fig. 7(c)]. This enhancement can be obtained by simply detuning the etched hole sizes as shown in Fig. 1(f2) and Fig. 1(f3). For the band structure shown in Fig. 7(c), we have taken a detuning ratio $D/D' = 1.1$.

If the detuning is increased again, the band structure tends in a continuous manner towards a kagome one [Figs. 7(d)–7(f)]. One can easily see in Fig. 1(f) that if $D' \ll D$, the system becomes a kagome one as in Fig. 1(c) (i.e., a hexagonal arrangement of large holes surrounded by six smaller ones). The six artificial atoms per unit cell in the structure of Fig. 1(f) merge two by two to give the three artificial atoms of the kagome lattice, resulting in a division of the s sector in s and p ones, the p states resulting from the antibonding combination of two neighboring s states. For example, for $D/D' = 2.7$ the band structure of the kagome lattice is recovered [Fig. 7(f) is formally similar to Fig. 6(a)].

This approach gives a new way of seeing the band structure of such lattices. Even though both graphene and kagome share a hexagonal symmetry, the link between their energy dispersion in the effective lattice Hamiltonian is not obvious.

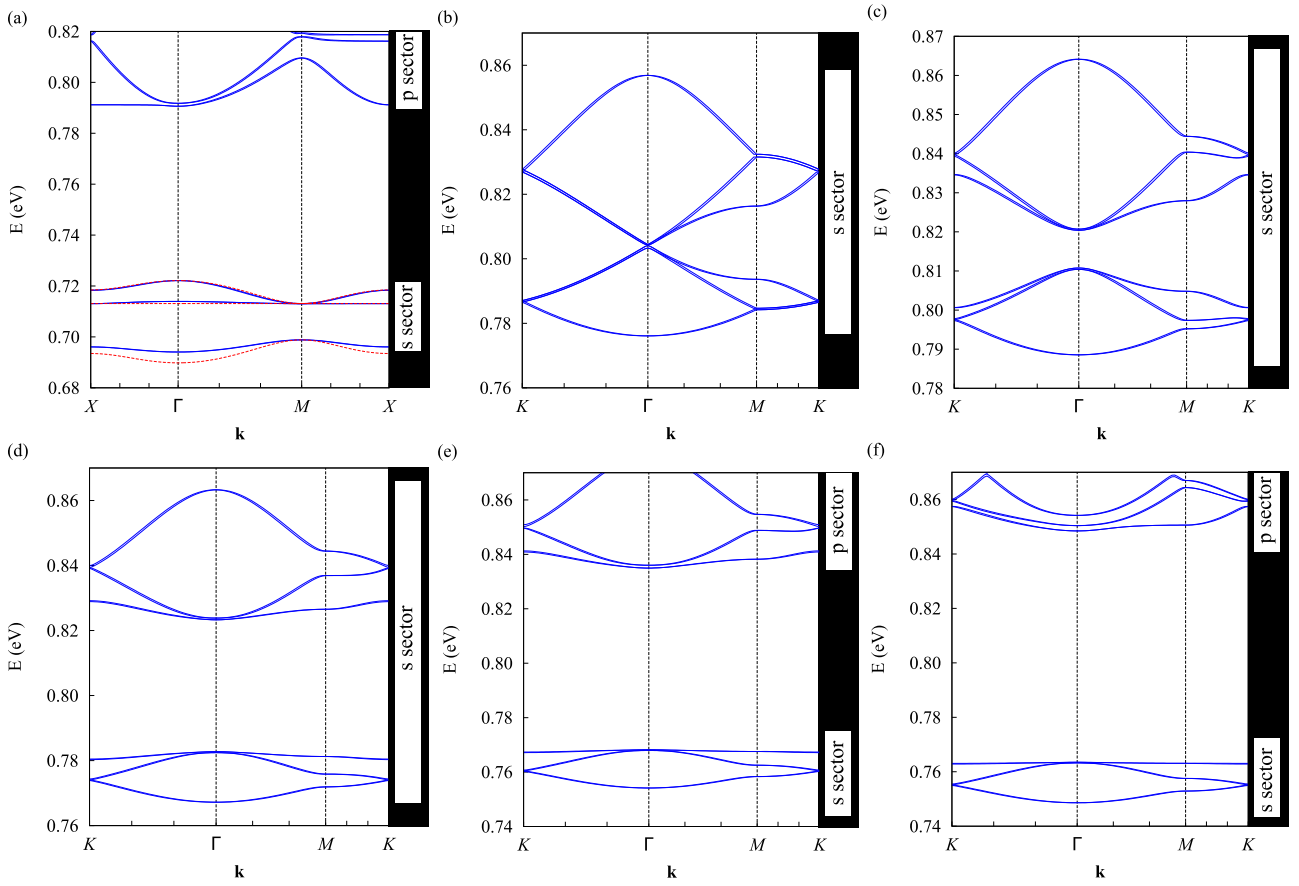

FIG. 7. Results for Lieb and detuned honeycomb superlattices made from an InAs film. (a) Lowest conduction bands for the Lieb superlattice with $d = 12.1$ nm, $D = 15.3$ nm, $D' = 7.6$ nm, and $t = 6.1$ nm. The path of the wave vector $\mathbf{k}$ in the Brillouin zone is depicted in Appendix B. The dashed lines in the s sector show the results of the effective Hamiltonian. (c) Lowest conduction bands for the detuned honeycomb superlattice with $d = 14.0$ nm, $D' = 10.5$ nm, $D = 11.6$ nm ($D/D' = 1.1$), and $t = 3.9$ nm. (b) Lowest conduction bands for the honeycomb superlattice with $d = 14.0$ nm, $D = D' = 10.5$ nm, and $t = 3.9$ nm represented in the same Brillouin zone as for the detuned one. (d) Same as (c) with $D' = 8.9$ nm and $D = 13.1$ nm ($D/D' = 1.5$). (e) Same as (c) with $D' = 7.3$ nm and $D = 14.6$ nm ($D/D' = 2.0$). (f) Same as (c) with $D' = 6.0$ nm and $D = 16.0$ nm ($D/D' = 2.7$).

Not only does the lithographic approach enlighten the relation between their band structures, it should also allow us to study the evolution of their properties when one goes from graphene to kagome lattice and vice versa, which is of course impossible with the real atomic lattices.

VI. REALIZATION OF THE POTENTIAL MODULATIONS USING InAs/AlSb

In all our previous calculations, we passivated the surfaces with pseudo-hydrogen atoms that form an artificial potential barrier. Experimentally, this confining barrier can be obtained by the use of oxides [54–56]. Although oxides are largely used in device technology, a high density of electronic states at the interface with III-V semiconductors is problematic for our purpose [57]. We propose here to use semiconductor heterojunctions instead, and we suggest the system InAs/AlSb as a promising case.

InAs/AlSb heterostructures have been widely studied for their high carrier mobility [58–60]. AlSb forms a natural barrier of 1.35 eV for electrons with 1.3% lattice mismatch between InAs and AlSb. We propose to fill the etched holes by epitaxial regrowth of AlSb after the lithography patterning, few layers of AlSb should also be grown under and on top of the InAs film to completely surround it with the barrier material [Fig. 8(a)].

Results of the calculation for a honeycomb InAs/AlSb heterostructure are shown in Figs. 8(b) and 8(c), for two different sizes. The AlSb barrier is high enough to efficiently confine the electrons and to recover the band structure obtained with the pseudo-hydrogen atom passivation. In fact, the band structure of Fig. 8(c) completely matches the one of Fig. 3(a), which is obtained for the same hole sizes.

VII. BILAYER ARTIFICIAL GRAPHENE

Besides monolayer graphene, bilayer graphene was also intensively studied in recent years [61–71]. Two different stackings are possible, the AA stacking where the two layers are superposed in a perfectly aligned manner, and the AB stacking where one of the layers is translated along a first-nearest-neighbor bond. The AA stacking was theoretically predicted to be structurally unstable [72,73]. Nevertheless, some theoretical investigations were made on this system and have shown promising properties such as Klein tunneling and spin Hall effect [74–80].

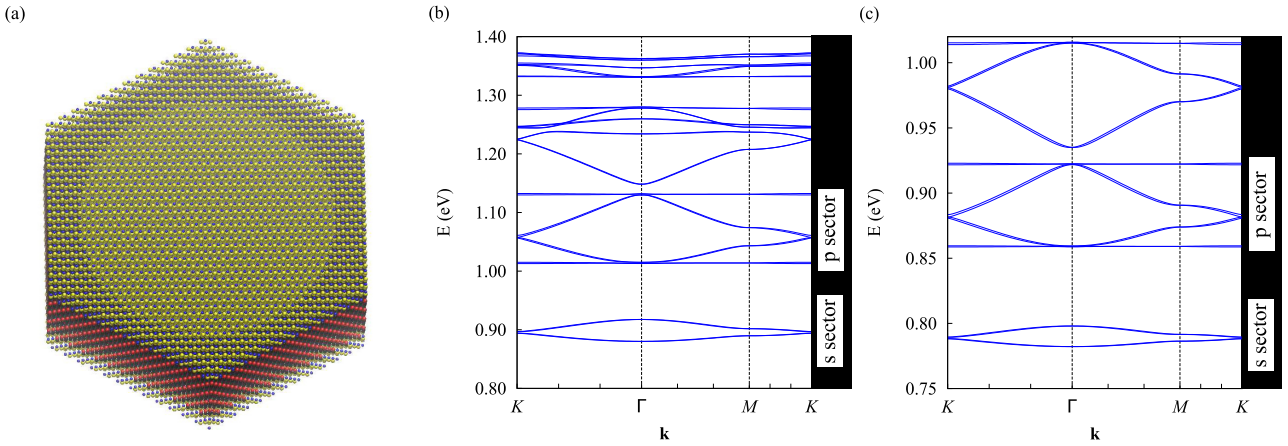

FIG. 8. Results for honeycomb superlattices realized with InAs/AlSb heterostructures. (a) Oblique view of the InAs/AlSb heterostructure: the etched holes in the InAs film are filled with AlSb. Top and bottom surfaces are passivated with few layers of AlSb. AlSb surfaces are passivated with hydrogen atoms (not shown). In atoms are in red, As atoms are in black, Al atoms are in yellow, Sb atoms are in blue. (b) Lowest conduction bands for $d = 16.0\,\text{nm}$, $D = 12.8\,\text{nm}$, and $t = 3.9\,\text{nm}$. (c) Lowest conduction bands for $d = 24.6\,\text{nm}$, $D = 19.7\,\text{nm}$, and $t = 3.9\,\text{nm}$.

By alternating AlSb and InAs layers before etching the hexagonal lattice holes, it is possible to create an AA bilayer artificial graphene [Fig. 9(a)]. As in the previous section, we assume a regrowth of AlSb after the etching in order to fill the holes with the barrier material.

The AA stacked graphene spectrum consists of a duplicated graphene band structure separated in energy by 2γ, where γ is the interlayer coupling. The dispersion relation of the π-π^* bands is written as [1]

$$E_{\pm}(\mathbf{k}) = E_s \pm t\sqrt{3 + f(\mathbf{k})} \tag{3}$$

with $f(\mathbf{k}) = \cos(\sqrt{3}k_y a) + 4\cos(\frac{\sqrt{3}}{2}k_y a)\cos(\frac{3}{2}k_x a)$, where E_s is the on-site energy, t the first-nearest-neighbor hopping energy, and a the lattice parameter.

Figure 9(c) shows the electron band structure of the system. In the s sector, the duplicated π-π^* bands of the monolayer artificial graphene are found as expected. A good agreement is found with the effective Hamiltonian (see Appendix D for the fitted parameters).

To verify that the energy splitting takes its origin from the coupling of the two monolayers ($\Delta E = 2\gamma$), we develop hereafter a simple model. Assuming that γ is proportional to the tunneling probability through the AlSb layer, we write

$$\gamma \propto e^{-\frac{\sqrt{2m^*(V-E_s)}}{\hbar}d'} \equiv e^{-\alpha d'}, \tag{4}$$

where d' is the distance between the two layers (i.e., the thickness of the AlSb interlayer), V is the potential barrier, E_s is the energy of the artificial s state, and m^* is the effective electron mass in the barrier material. The exponential fit of Fig. 9(b)

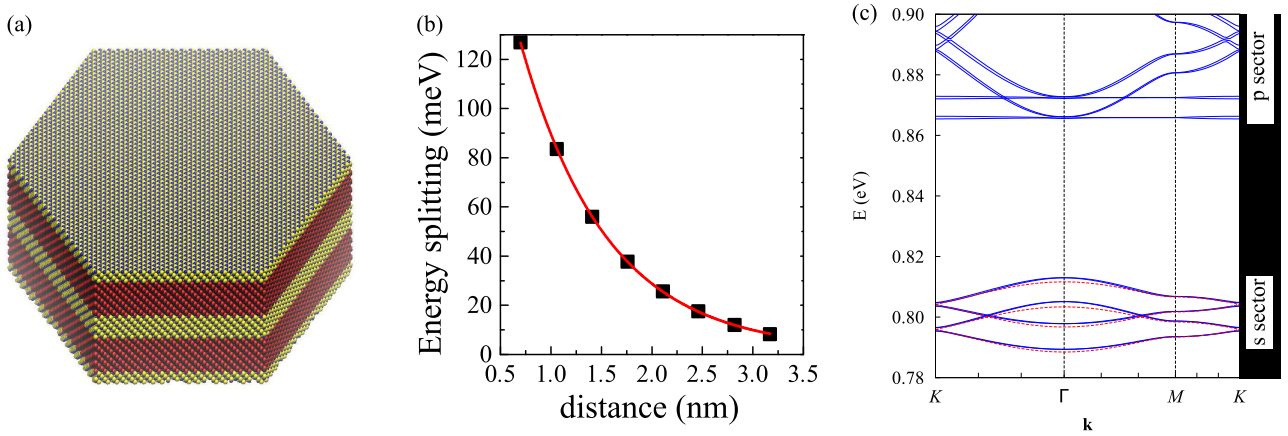

FIG. 9. Results for the AA stacked artificial graphene realized with InAs/AlSb heterostructures. (a) Oblique view of the AA stacked InAs/AlSb heterostructure: the etched holes in the two InAs films and the interlayer between them are filled with AlSb. Top and bottom surfaces are passivated with few layers of AlSb. AlSb surfaces are passivated with hydrogen atoms (not shown). In atoms are in red, As atoms are in black, Al atoms are in yellow, Sb atoms are in blue. (b) Evolution of the energy splitting (■) between the two Dirac points in the s sector vs the thickness d' of the AlSb interlayer between the two InAs quantum wells. The solid line is a numerical fit assuming a splitting varying like $\exp(-\alpha d')$. (c) Lowest conduction bands for $d = 24.6\,\text{nm}$, $D = 19.7\,\text{nm}$, $d' = 3.2\,\text{nm}$, and $t = 3.9\,\text{nm}$. The dashed lines in the s sector show the results of the effective Hamiltonian.

TABLE I. TB parameters (notations of Slater and Koster [85]) for InSb in an orthogonal $sp^3d^5s^*$ model. Δ is the spin-orbit coupling. (a) and (c) denote the anion (Sb) and the cation (In), respectively. Lattice parameter: $a = 6.4793$ Å.

Parameters for InSb (eV)			
E_s(a)	−5.55828		
E_s(c)	0.52753		
E_p(a)	2.74743	E_p(c)	4.54895
E_d(a)	11.51822	E_d(c)	11.51822
E_{s^*}(a)	18.43176	E_{s^*}(c)	18.43176
Δ(a)	0.44950	Δ(c)	0.12300
$V_{ss\sigma}$(ac)	−1.12227	$V_{s^*s^*\sigma}$(ac)	−4.30235
$V_{ss^*\sigma}$(ac)	−1.88189	$V_{ss^*\sigma}$(ca)	−2.00420
$V_{sp\sigma}$(ac)	2.50841	$V_{sp\sigma}$(ca)	2.65119
$V_{s^*p\sigma}$(ac)	2.73800	$V_{s^*p\sigma}$(ca)	2.34710
$V_{sd\sigma}$(ac)	−2.45802	$V_{sd\sigma}$(ca)	−2.77740
$V_{s^*d\sigma}$(ac)	−0.73710	$V_{s^*d\sigma}$(ca)	−0.81440
$V_{pp\sigma}$(ac)	3.48365	$V_{pp\pi}$(ac)	−1.23018
$V_{pd\sigma}$(ac)	−1.65148	$V_{pd\sigma}$(ca)	−1.73100
$V_{pd\pi}$(ac)	1.56926	$V_{pd\pi}$(ca)	1.65149
$V_{dd\sigma}$(ac)	−1.30520	$V_{dd\pi}$(ac)	2.07840
$V_{dd\delta}$	−1.41180		
Parameters for In-H and Sb-H (eV)			
E_H	3.91350		
$V_{ss\sigma}$	−34.34193	$V_{sp\sigma}$	45.13511

gives $\alpha = 1.17\,\mathrm{nm}^{-1}$. If we take $V = 1.35$ eV and $E_s = 0.789$ eV as given in Fig. 8(c) by the position of the Dirac cone at the K point, we have $m^* = 0.093m_0$ where m_0 is the electron mass. This result is close to the common values ($\approx 0.1m_0$) used in literature for the electron effective mass in AlSb [41,81–83], and close to the effective mass ($0.109\ m_0$) at Γ derived from the tight-binding parametrization that we use in the present work [41]. Thus, the obtained electronic structure really derives from the coupling of two artificial graphene monolayers.

VIII. CONCLUSION

In conclusion, we have theoretically investigated the electronic band structure of superlattices, which could be realized by lithographic techniques in ultrathin films of III-V and II-VI semiconductors. By designing artificial lattices, it is possible to create 2D materials characterized by band structures, which were previously studied on the basis of effective tight-binding models. Dirac cones, nontrivial flat bands, and band crossing points can be found not only in artificial graphene but also in more exotic lattices, such as kagome, Lieb, and distorted honeycomb, demonstrating the possibility to play with the geometry and the topology. The performed study on AA bilayer graphene, which is unstable in its atomic form, opens a road towards designing artificial structures that present interesting features but are unfortunately unstable in their real atomic form. In a more general view, we hope that this work will motivate the experimental realization of quantum systems, which have only been studied so far using model Hamiltonians. This is clearly challenging, for example, regarding the effects of disorder, but within reach using present technological means for the lattice dimensions that we have considered.

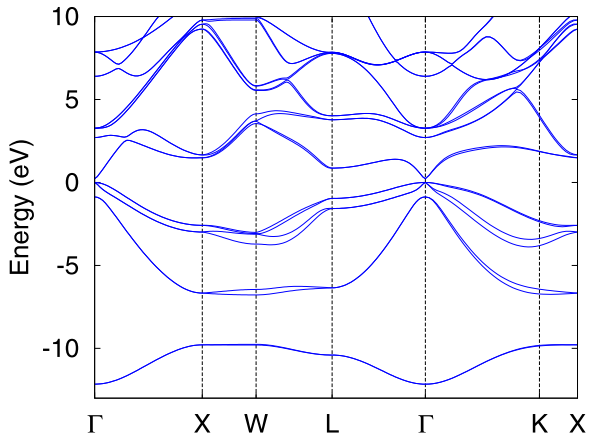

FIG. 10. Band structure of InSb calculated in TB using the parameters of Table I. The zero of energy corresponds to the top of the valence band.

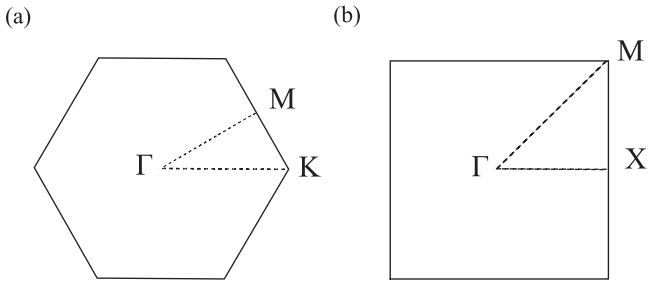

FIG. 11. Brillouin zones of all studied structures. (a) Triangular lattice Brillouin zone with its high symmetry points that corresponds to honeycomb, kagome, distorted, and detuned honeycomb superlattices. (b) Square lattice Brillouin zone with its high symmetry points that corresponds to square and Lieb superlattices.

ACKNOWLEDGMENTS

A.T. and C.D. acknowledge very fruitful discussions with D. Vanmaekelbergh, B. Grandidier, D. Stiévenard, X. Wallart, and L. Desplanque. The atomic figures were obtained using the open software VMD [84]. G.A. and C.D. thank K. Hummer for providing the accurate band structure of bulk InSb calculated using hybrid functionals.

APPENDIX A: TIGHT-BINDING PARAMETERS FOR InSb

The electronic structure of InSb is calculated as described in Ref. [43] for Si and Ref. [86] for III-V materials. Only first-nearest-neighbor interactions are considered between two orbitals located on different atoms (hopping integrals). The

TABLE II. Effective tight-binding parameters for the distorted honeycomb. E_c, E_e, and E_v are the on-site energies of the center, edge, and vertex atoms, respectively. t_{v-e} is the hopping energy between a vertex and an edge atom and t_{c-e} is the hopping energy between a center and an edge one.

Parameters for the effective model (eV)					
E_c	0.810	E_v	0.794	t_{v-e}	−0.0130
E_e	0.807			t_{c-e}	−0.0040

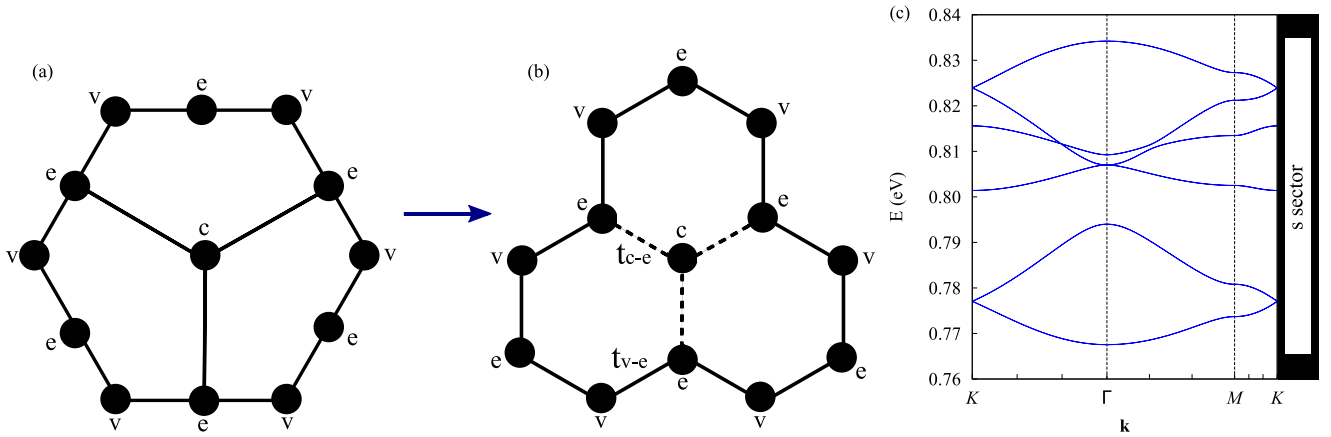

FIG. 12. From a distorted honeycomb to a detuned one. (a) Unit cell of the distorted honeycomb presented in Sec. V B and (b) its equivalent detuned honeycomb with two different hopping energies: t_{v-e} (solid lines) and t_{c-e} (dashed lines). The letters c, e, and v stand for center, edge, and vertex site respectively. (c) The band structure obtained with the effective tight-binding Hamiltonian.

atomistic tight-binding Hamiltonian is written as functions of parameters fitted in order to reproduce the band structure for the bulk system obtained with the *ab initio* calculations of Ref. [87]. We have considered a basis of $sp^3d^5s^*$ (s^* is a second s orbital) orbitals. The basis set is doubled in order to take into account spin-orbit coupling. The TB parameters are given in Table I, and the corresponding band structure is shown in Fig. 10. The TB parameters are obtained numerically using a conjugate gradient method, allowing us to get accurate positions of the bands at the main points of the Brillouin zone over a wide energy range (shown in Fig. 10), as well as correct effective masses at band edges. The terms E in Table I represent the on-site energies of orbitals, E_s being for example the s orbital energy in the solid. The terms V in Table I completely define the hopping matrix terms in the two-center approximation [85]. The In-H and Sb-H parameters are defined so the surface states are pushed far from the band edges. By convention, the zero of energy is taken at the top of the valence band.

APPENDIX B: BRILLOUIN ZONES AND FOLLOWED PATHS

We briefly present in this appendix the Brillouin zones of each studied structure (Fig. 11). For all structures with triangular superlattice symmetry, the followed path is $K \rightarrow \Gamma \rightarrow M \rightarrow K$. For square superlattice symmetry, the followed path is $X \rightarrow \Gamma \rightarrow M \rightarrow X$.

APPENDIX C: EFFECTIVE TIGHT-BINDING HAMILTONIAN FOR THE DISTORTED HONEYCOMB LATTICE

It is possible to consider the distorted honeycomb presented in Sec. V B as a detuned honeycomb, but with a detuning different than the one presented in Sec. V D. Figure 12 shows the distortion that transform the unit cell of the distorted honeycomb into a honeycomb. Thus, we can recover the band structure of the distorted honeycomb by using a modified honeycomb effective tight-binding Hamiltonian.

We consider an effective Hamiltonian with simple s orbitals per site and a hopping energy t. Due to the distortion, the center, edge, and vertex nanocrystals have different shapes. This can be modeled in the effective Hamiltonian by slightly different on-site energies E_c, E_e, E_v, respectively. Moreover, the distortion increases the distance between the central and edge atoms. This change can be modeled by considering two different hopping energies: a vertex-edge term (t_{v-e}) and a center-edge one (t_{c-e}).

Figure 12(c) shows the obtained band structure with the parameters presented in Table II. The band structure is close to the distorted honeycomb one [Fig. 6(b)]. The main difference is in the bandwidths of the π-π^* manifolds. This comes from the fact that we do not consider sp coupling terms and also that the envelope wave functions in the distorted honeycomb are not pure s states. Nevertheless, a very simple model is able to reproduce the main features of a complex band structure.

APPENDIX D: EFFECTIVE TIGHT-BINDING PARAMETERS FOR KAGOME, LIEB AND AA STACKED HONEYCOMB LATTICE

In this appendix, we report the fitted values for the effective tight binding in the case of kagome, Lieb, and AA stacked graphene lattice (see Sec. V and Sec. VII). Table III shows those values.

TABLE III. Effective tight-binding parameters for kagome, Lieb, and AA stacked graphene. t is the first-nearest-neighbor coupling term and γ is the interlayer coupling. In the case of kagome and AA stacked graphene, E_s is the s effective orbital on-site energy. In the case of the Lieb lattice, E_s is the mean on-site energy between edge and vertex sites and 2Δ is the difference between them.

Parameters for the effective model (meV)				
Lattice	E_s	t	γ	Δ
kagome	696.93	2.03		
Lieb	705.96	5.13		7.13
AA graphene	800.05	2.48	4.13	

[1] A. H. Castro Neto, F. Guinea, N. M. R. Peres, K. S. Novoselov, and A. K. Geim, Rev. Mod. Phys. **81**, 109 (2009).

[2] S. Z. Butler, S. M. Hollen, L. Cao, Y. Cui, J. A. Gupta, H. R. Gutirrez, T. F. Heinz, S. S. Hong, J. Huang, A. F. Ismach, E. Johnston-Halperin, M. Kuno, V. V. Plashnitsa, R. D. Robinson, R. S. Ruoff, S. Salahuddin, J. Shan, L. Shi, M. G. Spencer, M. Terrones, W. Windl, and J. E. Goldberger, ACS Nano **7**, 2898 (2013).

[3] M. Xu, T. Liang, M. Shi, and H. Chen, Chem. Rev. **113**, 3766 (2013).

[4] G. R. Bhimanapati, Z. Lin, V. Meunier, Y. Jung, J. Cha, S. Das, D. Xiao, Y. Son, M. S. Strano, V. R. Cooper, L. Liang, S. G. Louie, E. Ringe, W. Zhou, S. S. Kim, R. R. Naik, B. G. Sumpter, H. Terrones, F. Xia, Y. Wang, J. Zhu, D. Akinwande, N. Alem, J. A. Schuller, R. E. Schaak, M. Terrones, and J. A. Robinson, ACS Nano **9**, 11509 (2015).

[5] K. S. Novoselov, A. K. Geim, S. V. Morozov, D. Jiang, Y. Zhang, S. V. Dubonos, I. V. Grigorieva, and A. A. Firsov, Science **306**, 666 (2004).

[6] K. S. Novoselov, A. K. Geim, S. V. Morozov, D. Jiang, M. I. Katsnelson, I. V. Grigorieva, S. V. Dubonos, and A. A. Firsov, Nature (London) **438**, 197 (2005).

[7] S. Cahangirov, M. Topsakal, E. Aktürk, H. Şahin, and S. Ciraci, Phys. Rev. Lett. **102**, 236804 (2009).

[8] M. Polini, F. Guinea, M. Lewenstein, H. C. Manoharan, and V. Pellegrini, Nature Nano. **8**, 625 (2013).

[9] C.-H. Park and S. G. Louie, Nano Lett. **9**, 1793 (2009).

[10] M. Gibertini, A. Singha, V. Pellegrini, M. Polini, G. Vignale, A. Pinczuk, L. N. Pfeiffer, and K. W. West, Phys. Rev. B **79**, 241406 (2009).

[11] A. Singha, M. Gibertini, B. Karmakar, S. Yuan, M. Polini, G. Vignale, M. I. Katsnelson, A. Pinczuk, L. N. Pfeiffer, K. W. West, and V. Pellegrini, Science **332**, 1176 (2011).

[12] G. D. Simoni, A. Singha, M. Gibertini, B. Karmakar, M. Polini, V. Piazza, L. N. Pfeiffer, K. W. West, F. Beltram, and V. Pellegrini, Appl. Phys. Lett. **97**, 132113 (2010).

[13] L. Nádvorník, M. Orlita, N. A. Goncharuk, L. Smrčka, V. Novák, V. Jurka, K. Hruška, Z. Výborný, Z. R. Wasilewski, M. Potemski, and K. Výborný, New J. Phys. **14**, 053002 (2012).

[14] D. Scarabelli, S. Wang, A. Pinczuk, S. J. Wind, Y. Y. Kuznetsova, L. N. Pfeiffer, K. West, G. C. Gardner, M. J. Manfra, and V. Pellegrini, J. Vac. Sci. Technol. B **33**, 06FG03 (2015).

[15] W. H. Evers, B. Goris, S. Bals, M. Casavola, J. de Graaf, R. van Roij, M. Dijkstra, and D. Vanmaekelbergh, Nano Lett. **13**, 2317 (2013).

[16] M. P. Boneschanscher, W. H. Evers, J. J. Geuchies, T. Altantzis, B. Goris, F. T. Rabouw, S. A. P. van Rossum, H. S. J. van der Zant, L. D. A. Siebbeles, G. Van Tendeloo, I. Swart, J. Hilhorst, A. V. Petukhov, S. Bals, and D. Vanmaekelbergh, Science **344**, 1377 (2014).

[17] C. Delerue and D. Vanmaekelbergh, 2D Mater. **2**, 034008 (2015).

[18] E. Kalesaki, C. Delerue, C. Morais Smith, W. Beugeling, G. Allan, and D. Vanmaekelbergh, Phys. Rev. X **4**, 011010 (2014).

[19] C. Delerue, Phys. Chem. Chem. Phys. **16**, 25734 (2014).

[20] W. Beugeling, E. Kalesaki, C. Delerue, Y.-M. Niquet, D. Vanmaekelbergh, and C. M. Smith, Nat. Commun. **6**, 6316 (2015).

[21] S.-L. Zhu, B. Wang, and L.-M. Duan, Phys. Rev. Lett. **98**, 260402 (2007).

[22] V. Pardo and W. E. Pickett, Phys. Rev. Lett. **102**, 166803 (2009).

[23] F. Ouyang, S. Peng, Z. Liu, and Z. Liu, ACS Nano **5**, 4023 (2011).

[24] K. K. Gomes, W. Mar, W. Ko, F. Guinea, and H. C. Manoharan, Nature (London) **483**, 306 (2012).

[25] D. Malko, C. Neiss, F. Viñes, and A. Görling, Phys. Rev. Lett. **108**, 086804 (2012).

[26] H. Huang, W. Duan, and Z. Liu, New J. Phys. **15**, 023004 (2013).

[27] J. Wang, H. Huang, W. Duan, and Z. Liu, J. Chem. Phys. **139**, 184701 (2013).

[28] L.-C. Xu, R.-Z. Wang, M.-S. Miao, X.-L. Wei, Y.-P. Chen, H. Yan, W.-M. Lau, L.-M. Liu, and Y.-M. Ma, Nanoscale **6**, 1113 (2014).

[29] Y. Ma, Y. Dai, X. Li, Q. Sun, and B. Huang, Carbon **73**, 382 (2014).

[30] H.-M. Guo and M. Franz, Phys. Rev. B **80**, 113102 (2009).

[31] A. O'Brien, F. Pollmann, and P. Fulde, Phys. Rev. B **81**, 235115 (2010).

[32] R. A. Vicencio and M. Johansson, Phys. Rev. A **87**, 061803 (2013).

[33] V. Apaja, M. Hyrkäs, and M. Manninen, Phys. Rev. A **82**, 041402 (2010).

[34] R. Shen, L. B. Shao, B. Wang, and D. Y. Xing, Phys. Rev. B **81**, 041410 (2010).

[35] R. A. Vicencio, C. Cantillano, L. Morales-Inostroza, B. Real, C. Mejía-Cortés, S. Weimann, A. Szameit, and M. I. Molina, Phys. Rev. Lett. **114**, 245503 (2015).

[36] S. Mukherjee, A. Spracklen, D. Choudhury, N. Goldman, P. Öhberg, E. Andersson, and R. R. Thomson, Phys. Rev. Lett. **114**, 245504 (2015).

[37] N. Goldman, D. F. Urban, and D. Bercioux, Phys. Rev. A **83**, 063601 (2011).

[38] G. Palumbo and K. Meichanetzidis, Phys. Rev. B **92**, 235106 (2015).

[39] S. Xia, Y. Hu, D. Song, Y. Zong, L. Tang, and Z. Chen, Opt. Lett. **41**, 1435 (2016).

[40] G. van Miert and C. M. Smith, Phys. Rev. B **93**, 035401 (2016).

[41] J.-M. Jancu, R. Scholz, F. Beltram, and F. Bassani, Phys. Rev. B **57**, 6493 (1998).

[42] E. Groeneveld, C. Delerue, G. Allan, Y.-M. Niquet, and C. de Mello Donegá, J. Phys. Chem. C **116**, 23160 (2012).

[43] Y. M. Niquet, C. Delerue, G. Allan, and M. Lannoo, Phys. Rev. B **62**, 5109 (2000).

[44] O. P. Sushkov and A. H. Castro Neto, Phys. Rev. Lett. **110**, 186601 (2013).

[45] E. Kalesaki, W. H. Evers, G. Allan, D. Vanmaekelbergh, and C. Delerue, Phys. Rev. B **88**, 115431 (2013).

[46] C. Wu and S. Das Sarma, Phys. Rev. B **77**, 235107 (2008).

[47] D. L. Bergman, C. Wu, and L. Balents, Phys. Rev. B **78**, 125104 (2008).

[48] D. Green, L. Santos, and C. Chamon, Phys. Rev. B **82**, 075104 (2010).

[49] E. Tang, J.-W. Mei, and X.-G. Wen, Phys. Rev. Lett. **106**, 236802 (2011).

[50] T. Neupert, L. Santos, C. Chamon, and C. Mudry, Phys. Rev. Lett. **106**, 236804 (2011).

[51] K. Sun, Z. Gu, H. Katsura, and S. Das Sarma, Phys. Rev. Lett. **106**, 236803 (2011).

[52] W. Beugeling, J. C. Everts, and C. Morais Smith, Phys. Rev. B **86**, 195129 (2012).

[53] L.-H. Wu and X. Hu, Sci. Rep. **6**, 24347 (2016).

[54] R. Schwartz, R. Dockerty, and H. Thompson, Jr, Solid State Electron. **14**, 115 (1971).
[55] C. W. Wilmsen, L. G. Meiners, and D. A. Collins, Thin Solid Films **46**, 331 (1977).
[56] M. Yamaguchi, A. Yamamoto, H. Sugiura, and C. Uemura, Thin Solid Films **92**, 361 (1982).
[57] T. Mimura and M. Fukuta, IEEE Trans. Electron Devices **27**, 1147 (1980).
[58] L. Desplanque, D. Vignaud, and X. Wallart, J. Cryst. Growth **301-302**, 194 (2007).
[59] H. Blank, M. Thomas, K. C. Wong, and H. Kroemer, Appl. Phys. Lett. **69**, 2080 (1996).
[60] B. Shojaei, A. McFadden, J. Shabani, B. D. Schultz, and C. J. Palmstrøm, Appl. Phys. Lett. **106**, 222101 (2015).
[61] E. McCann and M. Koshino, Rep. Prog. Phys. **76**, 056503 (2013).
[62] W. Tao, G. Qing, L. Yan, and S. Kuang, Chin. Phys. B **21**, 067301 (2012).
[63] S. Lee, K. Lee, and Z. Zhong, Nano Lett. **10**, 4702 (2010).
[64] K. Yan, H. Peng, Y. Zhou, H. Li, and Z. Liu, Nano Lett. **11**, 1106 (2011).
[65] M. Sui, G. Chen, L. Ma, W.-Y. Shan, D. Tian, K. Watanabe, T. Taniguchi, X. Jin, W. Yao, D. Xiao, and Y. Zhang, Nature Phys. **11**, 1027 (2015).
[66] L. Ju, Z. Shi, N. Nair, Y. Lv, C. Jin, J. Velasco, Jr, C. Ojeda-Aristizabal, H. A. Bechtel, M. C. Martin, A. Zettl, J. Analytis, and F. Wang, Nature (London) **520**, 650 (2015).
[67] Y. Shimazaki, M. Yamamoto, I. V. Borzenets, K. Watanabe, T. Taniguchi, and S. Tarucha, Nature Phys. **11**, 1032 (2015).
[68] A. Kou, B. E. Feldman, A. J. Levin, B. I. Halperin, K. Watanabe, T. Taniguchi, and A. Yacoby, Science **345**, 55 (2014).
[69] K. Lee, B. Fallahazad, J. Xue, D. C. Dillen, K. Kim, T. Taniguchi, K. Watanabe, and E. Tutuc, Science **345**, 58 (2014).
[70] P. Maher, L. Wang, Y. Gao, C. Forsythe, T. Taniguchi, K. Watanabe, D. Abanin, Z. Papić, P. Cadden-Zimansky, J. Hone, P. Kim, and C. R. Dean, Science **345**, 61 (2014).
[71] B. N. Szafranek, G. Fiori, D. Schall, D. Neumaier, and H. Kurz, Nano Lett. **12**, 1324 (2012).
[72] A. L. Rakhmanov, A. V. Rozhkov, A. O. Sboychakov, and F. Nori, Phys. Rev. Lett. **109**, 206801 (2012).
[73] D. S. de la Pea, M. M. Scherer, and C. Honerkamp, Ann. Phys. (Berlin) **526**, 366 (2014).
[74] Y.-H. Ho, J.-Y. Wu, R.-B. Chen, Y.-H. Chiu, and M.-F. Lin, Appl. Phys. Lett. **97**, 101905 (2010).
[75] C. J. Tabert and E. J. Nicol, Phys. Rev. B **86**, 075439 (2012).
[76] R. Roldán and L. Brey, Phys. Rev. B **88**, 115420 (2013).
[77] M. Sanderson, Y. S. Ang, and C. Zhang, Phys. Rev. B **88**, 245404 (2013).
[78] A. Dyrdał and J. Barnaś, Solid State Commun. **188**, 27 (2014).
[79] Y. Mohammadi and B. A. Nia, Solid State Commun. **201**, 76 (2015).
[80] W. Wang, S. Xiao, and N. Asger Mortensen, Phys. Rev. B **93**, 165407 (2016).
[81] T. B. Boykin, Phys. Rev. B **56**, 9613 (1997).
[82] G. Klimeck, R. C. Bowen, T. B. Boykin, and T. A. Cwik, Superlattice Microst. **27**, 519 (2000).
[83] I. Vurgaftman, J. R. Meyer, and L. R. Ram-Mohan, J. Appl. Phys. **89**, 5815 (2001).
[84] W. Humphrey, A. Dalke, and K. Schulten, J. Mol. Graphics **14**, 33 (1996).
[85] J. C. Slater and G. F. Koster, Phys. Rev. **94**, 1498 (1954).
[86] G. Allan, Y. M. Niquet, and C. Delerue, Appl. Phys. Lett. **77**, 639 (2000).
[87] Y.-S. Kim, K. Hummer, and G. Kresse, Phys. Rev. B **80**, 035203 (2009).